PHYSICAL REVIEW E **92**, 011002(R) (2015)

Capillary solitons on a levitated medium

S. Perrard,[1,2] L. Deike,[1,3] C. Duchêne,[1] and C.-T. Pham[4]

[1]*Laboratoire Matière et Systèmes Complexes, Université Paris Diderot, CNRS UMR 7057, Bâtiment Condorcet, 10 rue Alice Domon et Léonie Duquet, F-75013 Paris, France, EU*

[2]*James Franck Institute and Department of Physics, The University of Chicago, Chicago, Illinois 60637, USA*

[3]*Scripps Institution of Oceanography, University of California San Diego, La Jolla, California 92093, USA*

[4]*Laboratoire d'Informatique pour la Mécanique et les Sciences de l'Ingénieur, Université Paris-Sud, CNRS UPR 3251, rue J. von Neumann, F-91405 Orsay Cedex, France, EU*

(Received 4 December 2014; published 20 July 2015)

A water cylinder deposited on a heated channel levitates on its own generated vapor film owing to the Leidenfrost effect. This experimental setup permits the study of the one-dimensional propagation of surface waves in a free-to-move liquid system. We report the observation of gravity-capillary waves under a dramatic reduction of gravity (up to a factor 30), leading to capillary waves at the centimeter scale. The generated nonlinear structures propagate without deformation and undergo mutual collisions and reflections at the boundaries of the domain. They are identified as Korteweg–de Vries solitons with negative amplitude and subsonic velocity. The typical width and amplitude-dependent velocities are in excellent agreement with theoretical predictions based on a generalized Korteweg–de Vries equation adapted to any substrate geometry. When multiple solitons are present, they interact and form a soliton turbulencelike spectrum.

DOI: 10.1103/PhysRevE.92.011002 PACS number(s): 47.35.Fg, 05.45.Yv, 68.03.Kn

Since their first observation by Russell on the water surface of a channel [1], solitons have been studied in a wide range of physical contexts, for instance, acoustics, hydrodynamical internal waves [2,3], and living systems, such as in the propagation of the pressure blood disturbance in arteries [4]. Korteweg and de Vries (KdV) provided the first theoretical description of solitonic waves through the so-called KdV equation [5–7], describing the propagation of noninteracting solitons by a balance between dispersion and nonlinear effects [8]. Solitons can be either supersonic or subsonic, depending on the sign of the curvature of the dispersion relation close to infinite wavelength [7]. A superposition of many propagating solitons forming a turbulent soliton state has also been encountered in various situations ranging from plasma waves [9,10] to crystalline solids [11]. In spite of the full integrable feature of such systems [12], the description of the dynamical and statistical properties of many interacting solitonic structures remains an open question.

At the surface of a liquid layer, solitons are observed in the shallow regime ($\Delta \gg H$) where Δ is the typical soliton width and H is the fluid depth. Most observed are supersonic solitons in the gravity-driven domain ($\Delta \gg \ell_c$), where $\ell_c = \sqrt{\sigma/g\rho}$ (with σ the surface tension, ρ the liquid density, and g the acceleration of gravity) is the capillary length which defines the transition scale between gravity and capillary dominating forces. Under Earth's gravity, ℓ_c is typically equal to a few millimeters.

Albeit predicted in the capillary-driven domain, the observations of subsonic solitons on a fluid layer remain scarce. When the depth of the fluid is millimetric or less, dissipative effects on the surface and in the bulk [13,14] quickly damp the capillary waves. One experiment reports their observation at the surface of a thin layer of mercury but for a limited range of amplitude [15]. By driving with a moving object, recent experiments have observed localized subsonic waves, but with a more complex spatial structure [16] described by a modified nonlinear Schrödinger equation [17].

In order to observe surface waves corresponding to subsonic solitons, we take advantage of the Leidenfrost effect. It provides a remarkable situation in which a liquid levitates over its own vapor film [18]. Using a curved substrate [19], a 100 mL water cylinder is levitated. Capillary waves are found to propagate along the levitated liquid cylinder, arising now up to the centimeter scale. An effective 30-fold reduction of gravitational effects in an on-Earth laboratory experiment is indeed observed. The generated localized structures are identified as subsonic KdV solitons driven by surface tension. Eventually, when multiple solitons are generated, they interact and a turbulentlike wave spectrum is observed, which might be assigned to soliton turbulence.

The experimental setup is displayed in Fig. 1(a). A cylinder of distilled water is set in levitation by the Leidenfrost effect [20] on a Dural channel of 45 cm length and 4 cm width, heated at a temperature $T_p = 280 \pm 10\,^{\circ}$C. The liquid has a quarter-pipe section. The liquid evaporation is compensated by a flow ($Q = 7$ mL/min) of simmering water poured into the levitating cylinder with a motorized syringe [21]. A steady volume of water in levitation (density $\rho = 960$ kg/m^3 and surface tension $\sigma = 50 \pm 10$ mN/m at $100\,^{\circ}$C) is then obtained with $W = 18 \pm 0.2$ mm for the width and with $h = 4.5 \pm 0.5$ mm for the depth. The cylinder is pinned at each extremity and one end can be set in oscillation by a mechanical shaker driven either with a periodic function of frequency f varying from 1 to 20 Hz or with short pulses to generate localized structures. We focus on the horizontal disturbance of the liquid width $\eta(x,t)$ [Fig. 1(a)]. The interface position $\eta(x,t)$ is recorded from above with a digital camera at 50 fps and numerically detected with an algorithm of contour detection based on the change in the color gradient. A movie of propagating solitons is shown in the Supplemental Material [22], together with the detected interface.

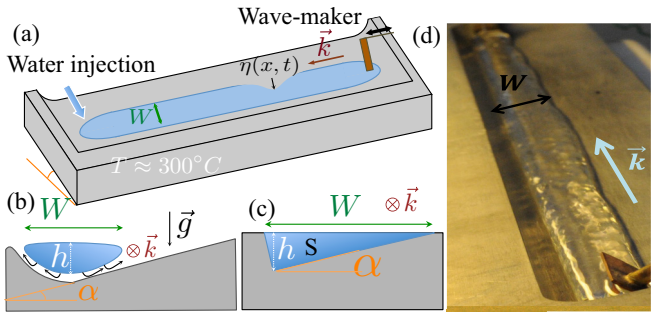

FIG. 1. (Color online) Sketch of the experimental setup. (a) 100 mL of distilled water is poured onto a 45 cm long quarter-pipe-shaped channel, heated at 280 °C, forming a levitated liquid cylinder. A wave maker is used to generate a disturbance $\eta(x,t)$ of the cylinder interface. (b) Side view of the channel: We focus on the propagation of waves along the free right-hand border of the interface. The inclination angle α of the container is tunable. (c) Sketch of the geometry investigated theoretically. (d) Photography of the experimental setup.

The originality of this setup comes from the channel geometry. At low inclination angle α of the channel with respect to the horizontal [see Fig. 1(b)], the motion of the left-hand liquid interface is limited by the substrate confinement. In contrast, the right-hand liquid interface is free to move along an almost horizontal plane and can undergo large variations. The liquid moving along $\mathbf{u}$ is subjected to a gravitational force through its projection $g' = \mathbf{g}\cdot\mathbf{u}$. It defines an effective gravity $g' = g\sin\alpha$. Experimentally, α can be tuned from a zero gravity situation ($\alpha \to 0, g' \to 0$) to a symmetric channel ($\alpha = 45°, g' \to g/\sqrt{2}$).

In this configuration, the wave propagation depends on the ratio between the fluid inertia per unit length ρS and the width W of the interface. The effective fluid depth H' for any cross section shape yields [23]

$$H' = \frac{S}{W\sin\alpha}. \tag{1}$$

The cross section [Fig. 1(b)] is modelized by a triangle [Fig. 1(c)] with an effective depth $H' = \frac{1}{2}\cos\alpha W$. This geometry is thus analogous to a one-dimensional water channel in which gravity g and fluid depth H can be tuned continuously simply by changing the inclination angle α. For instance, at an inclination angle $\alpha = 2°$, the effective gravity $g' = 0.34\ \mathrm{m\,s^{-2}}$ is 30 times smaller than usual.

Linear waves are characterized by exciting the water cylinder at 1 Hz. Figure 2 shows $S_\eta(k,\omega)$, the space-time spectral density of the liquid displacement $\eta(x,t)$, as a function of the wave number k and the angular frequency ω for an inclination angle $\alpha = 2°$. The energy is localized in Fourier space along two curves for ω ranging from 0.1 to 80 rad s^{-1}. While the driving is performed at low frequency, energy is observed in a large frequency range, stemming from nonlinear wave interactions leading to an energy cascade [24,25]. The lines of maximum energy density reveal the dispersion relations between k and ω. Two distinct branches are identified, corresponding to two propagation modes (I and II). The main branch (I) is a convex curve related to phase velocity

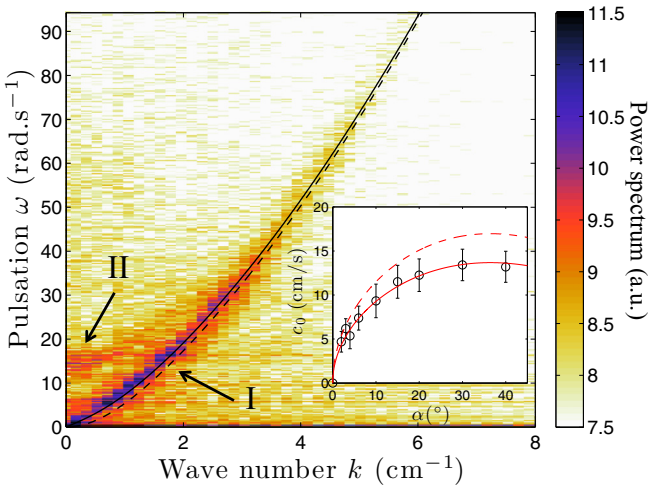

FIG. 2. (Color online) Power spectrum $S_\eta(k,\omega)$ of the cylinder right interface $\eta(x,t)$ for $\alpha = 2°$ as a function of k and ω. Color is log scaled. The energy is localized along two branches of propagation. I: Gravity-capillary waves given by Eq. (2) (solid line). The dashed line corresponds to the dispersion relation of pure capillary waves. II: Sloshing modes, i.e., in-phase oscillations of both the left- and right-hand sides of the interface. Inset: Experimental (○) minimum phase velocity c_0 as a function of α. c_0 is measured from a fit of the dispersion relation in the limit $k \to 0$. Theoretical model $c_0 = \sqrt{g'H'}$ [see Eq. (3)] with no fit parameter (dashed line) and with an adjusted geometrical factor $H_{\mathrm{eff}} = 0.65H'$ (solid line).

$c(k) = \omega/k$ ranging from 5 to 30 mm/s. It is associated with the variation of the cross section and therefore to deformations localized on the right interface, the left-hand side being almost unperturbed. The other branch (II) exhibits a frequency cutoff at $\omega_c = 14 \pm 1$ rad s^{-1}. This branch is related to a sloshing mode corresponding to an in-phase oscillation of both sides of the interface [26]. In the following, we solely focus on the main branch (I).

The main branch (I) is described by the usual dispersion relation for gravity-capillary waves,

$$\omega^2 = \Phi(H'k)\left(g'k + \frac{\sigma}{\rho}k^3\right), \tag{2}$$

where H' and g' are the effective depth and gravitational acceleration and $\Phi(x) = \tanh(x)$ for a rectangular channel [26]. Φ may, however, depend on the substrate shape. In our case, $\Phi(x) = \tanh(x)$ remains a good approximation in the whole range of tested inclination angles ($2° < \alpha < 45°$) (solid line in Fig. 2).

For $k > 1$ cm^{-1} the wave propagation is well described by the pure capillary wave dispersion relation ($\omega^2 = \sigma k^3/\rho$, dashed line in Fig. 2). The surface tension $\sigma = 35$ mN/m is, however, 30 % smaller than expected. The most likely origin of this discrepancy is the presence of contaminants at the surface. Other possible origins of this low surface tension value, such as the influence of a curved interface, still need to be investigated. The contamination process occurs during the first 30 min, at which time the surface tension reaches this asymptotic value. We choose to perform our measurements at a later time to ensure that σ remains constant during all the measurements. To avoid too much accumulation of

contaminants, the water is changed at least every 2 h. The effective capillary length computed with $g' = g\sin\alpha$ is larger than usual ($\ell_c^{\rm eff} = \sqrt{\sigma/\rho g'} \approx 1.2$ cm for $\alpha = 2^\circ$) due to the reduction of gravity.

In the limit $k \to 0$, the capillary term vanishes and gravity dominates. Using a section-averaged Saint-Venant equation [27] for inviscid fluid in the shallow water limit ($kH' \ll 1$) and neglecting capillarity ($k\ell_c \ll 1$), the nondispersive limit is recovered using the effective gravity g' and the effective depth H',

$$\omega^2 = g\frac{S}{W}k^2 = g'H'k^2, \tag{3}$$

where S and W designate the section and the cylinder width, respectively. The minimum phase velocity $c_0 = \omega/k$ is shown in the inset of Fig. 2 as a function of the inclination angle α. c_0 is in good agreement with its analytical expression deduced from Eq. (3) with a prefactor 20% smaller than expected. This discrepancy may be attributed to the difference between the experimental cross section [Fig. 1(b)] and the theoretical ansatz [Fig. 1(c)]. In the following, the effective depth $H_{\rm eff} = 0.65H'$ is used.

Close to $k = 0$, the leading dispersive contribution is found by expanding Eq. (2) to the fourth order in k. It yields

$$\omega^2 \simeq c_0^2k^2\left[1 + {H_{\rm eff}}^2({\rm Bo} - {\rm Bo_c})k^2\right], \tag{4}$$

where $c_0 = \sqrt{g'H_{\rm eff}}$ is the modified phase velocity for $k \to 0$ and ${\rm Bo_c} = -\Phi'''(0)/6$ is a critical Bond number. The amplitude and sign of the leading dispersive term strongly depends on the Bond number ${\rm Bo} \equiv (\ell_c^{\rm eff}/H_{\rm eff})^2$ which compares $H_{\rm eff}$ to the effective capillary length $\ell_c^{\rm eff}$.

When the dispersive effects are balanced by the nonlinear term in $\eta\eta_x$ [28], the propagation of nonlinear waves in the shallow limit ($kH_{\rm eff} \ll 1$) is described by a Korteweg–de Vries equation [5,7],

$$\eta_t + c_0\left[\eta_x + \frac{\mu_1}{H_{\rm eff}}\eta\eta_x + \frac{1}{2}H_{\rm eff}^2({\rm Bo_c} - {\rm Bo})\eta_{xxx}\right] = 0, \tag{5}$$

where $\mu_1 = 3/2$ for an uniform depth (rectangular channel). In the case of our geometrical ansatz, it can be shown that $\mu_1 = 5/2$ [23].

The sign of the dispersive term in η_{xxx} changes for a critical Bond number ${\rm Bo_c}$ (1/3 in the rectangular case). This limit separates two different types of solitons. Small Bond numbers ${\rm Bo} < {\rm Bo_c}$ correspond to supersonic gravity-driven waves, whereas large Bond numbers ${\rm Bo} > {\rm Bo_c}$ lead to the propagation of subsonic capillary-driven structures.

The shape of a gravity-capillary soliton can then be derived from the KdV equation (5),

$$\eta(x,t) = A_0\,{\rm sech}^2\left(\frac{x - ct}{\Delta}\right), \tag{6}$$

with A_0 the amplitude of the soliton, c its speed, and Δ its width. Both are related to the minimum of phase velocity c_0, the effective Bond number ${\rm Bo_{eff}}$, and the effective depth $H_{\rm eff}$,

$$c = c_0\left(1 + \frac{\mu_1 A_0}{3H_{\rm eff}}\right), \quad \Delta \equiv \sqrt{\frac{6({\rm Bo_c} - {\rm Bo})H_{\rm eff}^3}{\mu_1 A_0}}. \tag{7}$$

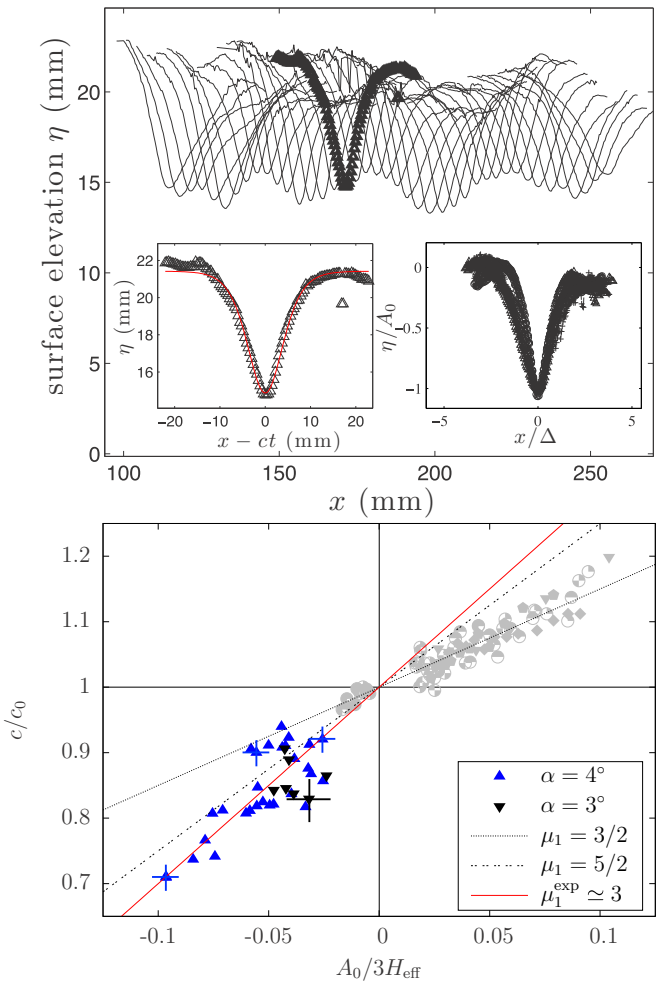

FIG. 3. (Color online) Top: $\eta(x,t)$ of a capillary soliton as a function of time (solid line) with a time step 0.04 s between two neighboring profiles ($\alpha = 4^\circ$). Left inset: Experimental data (Δ) and theoretical shape of a negative amplitude soliton given by Eq. (6) (solid red line). Right inset: Rescaling of the solitonic shape for various soliton amplitudes using the expression of Δ given by Eq. (7) ($\times$). Bottom: Normalized velocity c/c_0 as a function of the normalized amplitude $A_0/3H_{\rm eff}$ for $\alpha = 3^\circ$ and 4° and data from Falcon *et al.* [15] (gray symbols). Linear relations correspond to Eq. (7) for three theoretical values of μ_1 [flat channel $\mu_1 = 3/2$, triangular geometry in Fig. 1(c) $\mu_1 = 5/2$], and best experimental fit ($\mu_1 = 3 \pm 0.4$). Typical error bars are shown on four data points.

Figure 3 (top) shows the evolution of one depression soliton as a function of time. The shape is conserved during the propagation while its amplitude is modulated at low frequency by the sloshing modes. The amplitude slowly decreases with time due to dissipative effects. Its shape is given by Eq. (6) [left inset of Fig. 3 (top)]. The velocity c is measured from the position of the soliton minimum as a function of time. Individual interaction events with other solitons perturb briefly both the shape and the velocity but the speed remains constant between two of these events.

The right inset of Fig. 3 (top) shows the rescaled solitons $A/|A_0|$ as a function of $(x - ct)/\Delta$ for various initial pulses corresponding to negative amplitudes A_0 ranging from 2 to 5 mm. Since c, A_0, and W are measured and ${\rm Bo_{eff}}$ is known

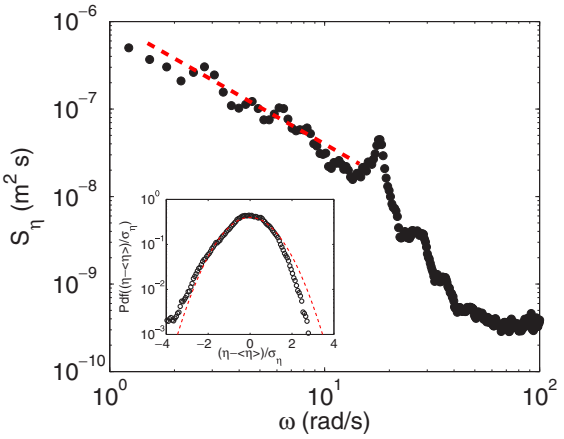

FIG. 4. (Color online) $S_\eta(\omega)$, calculated for each x location and then spatially averaged. A $\omega^{-1.5}$ power law (red dashed line) is observed at low ω, with a cutoff at $\omega = 18$ rad/s corresponding to the sloshing mode. This low frequency regime can be interpreted as a solitary wave turbulence regime. Inset: Normalized PDF of η. High amplitude negative events lead to a departure from the Gaussian statistics (red dashed line).

for a given α, there is no adjustable parameter. The rescaled data are found to be in good agreement with the theoretical shape. A typical soliton can undergo several reflections at the edges of the cylinder before being totally dissipated. Therefore, the typical dissipative scale is of the order of 1 m, which is 100 times larger than their sizes. The soliton velocity c/c_0 is plotted as a function of its normalized amplitude $A_0/3H_{\text{eff}}$ for several experiments of various driving amplitudes [Fig. 3 (bottom)]. All the observed solitons are subsonic, since $\text{Bo}_{\text{eff}} > \text{Bo}_c$. In addition, the speed decreases for larger negative amplitude. Straight lines correspond to $(c/c_0) = 1 + \mu_1(A_0/3H_{\text{eff}})$ for three values of μ_1. The classical rectangular case is given by $\mu_1 = 3/2$, and the case of our triangular ansatz corresponds to $\mu_1 = 5/2$. The best fit to our experimental data is slightly larger with $\mu_1 \simeq 3 \pm 0.4$, which is a 20% deviation from the triangular ansatz. Good quantitative agreement with the theoretical prediction is then obtained.

The observed range can be compared to a positive shallow water KdV soliton observed by Falcon *et al.* [15] [Fig. 3 (bottom)]. H_{eff} replaces the liquid depth H in Ref. [15]. Our results go far beyond these observations in the subsonic domain, reaching an amplitude limit that is almost the same as in the supersonic case ($|A/3H_{\text{eff}}| \approx 0.1$ and $|c - c_0|/c_0 \approx 0.3$). Note that the data at low ratio $A_0/3H_{\text{eff}} \approx 0.04$ are scattered due to the concomitance of linear waves of various frequencies.

When solitons are continuously generated, multiple solitary waves of various sizes and amplitudes are observed. Figure 4 shows the wave height power spectrum $S_\eta(\omega)$ as a function of ω. $S_\eta(\omega)$ follows a power law at low frequency, with $S_\eta(\omega) \sim \omega^{-\beta}$, and $\beta = 1.5$. The power law exponent is found to be roughly constant ($1 < \beta < 1.5$) for all tested driving amplitudes and low gravity cases ($\alpha < 4°$). This solitary wave turbulencelike regime is limited at high frequency by the sloshing frequency and at low frequency by the duration of the experiment. Interestingly, a similar regime has been recently reported for gravity-driven solitary waves in shallow water approaching the coast [29] and assigned to soliton turbulence, similar to a dense gas soliton turbulence [12]. Finally, the inset in Fig. 4 shows the probability density function (PDF) of the wave height. The wave statistic presents a clear asymmetry, related to the capillary wave asymmetry, together with a departure from the Gaussian statistics, due to the occurrence of numerous nonlinear solitons of negative large amplitude.

We thank J. Haddad and L. Dupuy for performing preliminary experiments; A. Lantheaume for technical assistance; and E. Fort, L. Limat, Y. Couder, and E. Falcon for helpful discussions. This work was supported by the French Agence Nationale de la Recherche through Grant No. ANR-11-BS04-001-01 (FREEFLOW Project).

[1] J. Russel, York 1844 BA Reports, pp 311–390 (1845).
[2] C. G. Koop and G. Butler, J. Fluid Mech. **112**, 225 (1980).
[3] J. W. Miles, Tellus **31**, 456 (1979).
[4] S. Yomosa, J. Phys. Soc. Jpn. **56**, 506 (1987).
[5] L. J. W. S. Rayleigh, Philos. Mag. **1**, 257 (1876).
[6] J. Boussinesq, C. R. Acad. Sci., Paris **72**, 755 (1871).
[7] D. Korteweg and G. de Vries, Philos. Mag. J. Sci. **39**, 422 (1895).
[8] R. K. Dodd, J. C. Eilbeck, J. D. Gibbon, and H. C. Morris, *Solitons and Nonlinear Wave Equations* (Academic, New York, 1982).
[9] H. Ikezi, R. J. Taylor, and D. R. Baker, Phys. Rev. Lett. **25**, 11 (1970).
[10] S. Ghosh, Europhys. Lett. **99**, 36002 (2012).
[11] H.-Y. Hao and H. J. Maris, Phys. Rev. B **64**, 064302 (2001).
[12] V. E. Zakharov, Stud. Appl. Math. **122**, 219 (2009).
[13] W. G. V. Dorn, J. Fluid Mech. **24**, 769 (1966).
[14] J. W. Miles, Proc. R. Soc. London, Ser. A **297**, 459 (1967).
[15] E. Falcon, C. Laroche, and S. Fauve, Phys. Rev. Lett. **89**, 204501 (2002).
[16] J. Diorio, Y. Cho, J. H. Duncan, and T. R. Akylas, Phys. Rev. Lett. **103**, 214502 (2009).
[17] Y. Cho, J. D. Diorio, T. R. Akylas, and J. H. Duncan, J. Fluid Mech. **672**, 288 (2011).
[18] D. Quéré and A. Ajdari, Nat. Mater. **5**, 429 (2006).
[19] S. Perrard, Y. Couder, E. Fort, and L. Limat, Europhys. Lett. **100**, 54006 (2012).
[20] J. G. Leidenfrost, *De Aquae Communis Nonnullis Qualitatibus Tractatus* (Ovenius, Duisburg, 1756).
[21] A.-L. Biance, C. Clanet, and D. Quéré, Phys. Fluids **15**, 1632 (2003).
[22] See Supplemental Material at http://link.aps.org/supplemental/10.1103/PhysRevE.92.011002 for a movie showing a collision between two capillary solitons.

[23] C. T. Pham (private communication).
[24] E. Falcon, C. Laroche, and S. Fauve, Phys. Rev. Lett. **98**, 094503 (2007).
[25] M. Berhanu and E. Falcon, Phys. Rev. E **87**, 033003 (2013).
[26] H. Lamb, *Hydrodynamics* (Cambridge University Press, Cambridge, UK, 1932).
[27] A. Decoene, L. Bonaventura, E. Miglio, and F. Saleri, Math. Models Methods Appl. Sci. **19**, 387 (2009).
[28] T. Dauxois and M. Peyrard, *Physics of Solitons* (Cambridge University Press, Cambridge, UK, 2006).
[29] A. Costa, A. R. Osborne, D. T. Resio, S. Alessio, E. Chrivì, E. Saggese, K. Bellomo, and C. E. Long, Phys. Rev. Lett. **113**, 108501 (2014).